Shells in a toroidal nucleus in the intermediate-mass region

Cheuk-Yin Wong*
Physics Division, Oak Ridge National Laboratory, Oak Ridge, Tennessee 37831, USA

Andrzej Staszczak†
Institute of Physics, Maria Curie-Skłodowska University, pl. M. Curie-Skłodowskiej 1, 20-031 Lublin, Poland

(Received 14 June 2018; revised manuscript received 31 July 2018; published 19 September 2018)

Attention is fixed on shells in toroidal nuclei in the intermediate-mass region using a toroidal single-particle potential. We find toroidal shells in the intermediate-mass region with large single-particle energy gaps at various nucleon numbers. These toroidal shells are located at different toroidal deformations characterized by the aspect ratios of the toroidal major radius to the toroidal minor radius, and they provide extra stability at various toroidal deformations. Relative to a toroidal core, the Bohr–Mottelson spin-aligning particle-hole excitations may be constructed to occupy the lowest single-particle Routhian energies to lead to toroidal high-spin isomers with different spins. Furthermore, because a nucleon in a toroidal nucleus possesses a vorticity quantum number, toroidal vortex nuclei may be constructed by making particle-hole excitations in which nucleons of one type of vorticity are promoted to populate unoccupied single-particle orbitals of the opposite vorticity. Methods for producing toroidal high-spin isomers and toroidal vortex nuclei are discussed.

DOI: 10.1103/PhysRevC.98.034316

I. INTRODUCTION

Wheeler suggested that, under appropriate conditions, the nuclear fluid may assume the shape of a torus [1]. Favorable conditions include nuclear-shell effects [2,3], large Coulomb energies [2–4], large nuclear angular momenta [5–8], nuclear collision dynamics [9,10], and combinations thereof. Although the basic ideas on the conditions favorable for toroidal configurations were presented many decades ago [2–10], the subject matter has gained renewed interest recently because powerful theoretical and experimental tools are now readily available [11–39]. The interest is heightened by recent experimental evidence for the presence of resonances at high excitation energies in the 7α disassembly of ^{28}Si, which may suggest the production of toroidal high-spin isomers predicted in many theoretical calculations [28]. Should these experimental results be confirmed by further studies, toroidal nuclei would potentially be interesting objects of study because of their new form of geometry, new toroidal shells and magic numbers, new types of yrast high-spin states, new toroidal nuclei species in different mass regions, new probes of nuclear energy density functional and nuclear equations of state in a new density regime, and new possible doorways to energy-producing mechanisms.

It is instructive to see how nuclear-shell effects and the alignment of single-particle spins along the symmetry axis can constrain the nucleus to assume a toroidal shape. We characterize the toroidal deformation of a toroidal nucleus by the aspect ratio R/d of the major radius R to the minor radius d. For light nuclei, there are large energy gaps in toroidal single-particle energies in an extended region of toroidal deformations. These energy gaps give rise to "toroidal shells" at "magic" nucleon numbers $N = 2(2m + 1)$, with integers $m \geqslant 1$ [2,3]. The extra stability associated with toroidal shells [40] leads to toroidal local energy minima for many light nuclei. Toroidal excited (diabatic) states have been predicted for Ca to Ge, with mass numbers $40 \lesssim A \lesssim 70$ by using the Strutinsky shell correction method [2,3], and for ^{24}Mg [14] and ^{28}Si [28] by using a self-consistent relativistic mean-field theory. Relative to a toroidal core, spin-aligning Bohr–Mottelson particle-hole excitations occupying the lowest Routhian single-particle energies [41] can be constructed to yield a toroidal nucleus with a spin as a yrast state, by promoting nucleons with angular momentum aligned opposite to a chosen symmetry z axis to populate orbitals with angular momentum aligned along the symmetry z axis [15–20]. A spinning toroidal nucleus possesses an effective "rotational" energy, which tends to expand the toroid, whereas the energy associated with the nuclear bulk properties tends to contract the toroid. The balance between the two energies gives rise to a local toroidal energy minimum [4]. Self-consistent calculations have been carried out to locate toroidal high-spin isomers as yrast states in the light-mass region [15–20,28].

For the heavy and superheavy nuclei there is similarly a toroidal shell region with negative shell corrections [2,3]. The toroidal configuration is further favored by large Coulomb energies. As a consequence, many toroidal nuclei have been theoretically located in the superheavy region [11–13,25–27,29]. In situations where the $I = 0$ state in the toroidal nucleus ^{304}120 are not stable adiabatically, the spin-aligning Bohr–Mottelson particle-hole excitations generate yrast high-spin states to lead to adiabatic local energy minima at various

*wongc@ornl.gov
†andrzej.staszczak@poczta.umcs.lublin.pl

spin values [25,26]. The neighboring even-even $N = 184$ isotone nuclei with $Z = 118$ and 122, as well as the $Z = 120$ isotopes with $N = 182$ and 186, also possess toroidal high-spin isomers at various spins and toroidal deformations [27].

Along with theoretical predictions [2,3,11–20,25–27,29] and experimental investigations [28] in the light and heavy-mass regions, it is natural to ask whether toroidal nuclei may also be possible in the intermediate-mass region. In this regard, our knowledge of toroidal nuclei in this mass region is scanty. We wish to examine here toroidal shells in the intermediate-mass region with $30 \lesssim N$ (or Z) $\lesssim 96$ where negative shell corrections are present over an extended region of nucleon numbers and toroidal deformations [3]. A large number of toroidal shells at various toroidal deformations are expected. We would like to know whether there are some regularities in the shell structure, how frequent toroidal shells occur, what are their nucleon numbers, and where their corresponding toroidal deformations are located. Furthermore, Bohr–Mottelson spin-aligning particle-hole excitations relative to a toroidal core can lead to high-spin toroidal isomers, and these high-spin isomers as yrast states have longer lifetimes and a better chance of being detected [28]. We would like to examine the possibilities of toroidal high-spin isomers in this mass region by studying the shell structure of single-particle Routhian energies as a function of the cranking frequency. Such information will guide our intuition and help our search for toroidal excited states and toroidal high-spin isomers in future experiments and mean-field calculations in the intermediate-mass region.

In the present survey over a large extended multidimensional space of nucleon numbers N, toroidal deformations R/d, and nuclear spins $I = I_z$, it is convenient to use a simple harmonic-oscillator toroidal shell model for which the relevant results can be readily obtained. Furthermore, the simple toroidal shell model has the desirable property that many physical properties can be clearly exhibited. In particular, from the single-particle wave functions for the two-dimensional harmonic oscillators in the meridian plane, one finds that a nucleon in a toroidal nucleus possesses a vorticity quantum number $\Lambda_\perp$ associated with a circulating current around the poloidal angle θ (Fig. 1). We propose the possibility of toroidal vortex nuclei by making vortex-creating single-particle particle-hole excitations that promote nucleons of one type of vorticity from occupied orbitals to populate unoccupied single-particle orbitals of the opposite vorticity. The resultant nucleus will have a net nonzero vorticity $\Lambda_\perp$ as shown in Fig. 1. Because vorticity is quantized and cannot be easily destroyed, the presence of a net vorticity may enhance the stability of the toroidal vortex nucleus.

It should, however, be noted that the vorticity quantum number is nonzero only if the principal quantum number n of the two-dimensional harmonic-oscillator wave function for the nucleon motion on the meridian plane is greater than or equal to unity. This excludes the light toroidal nuclei from the possibility of becoming toroidal vortex nuclei.

Experiments have been performed recently to search for a toroidal high-spin isomer in ^{28}Si with spin $I = I_z = 44$ predicted earlier in Ref. [17] by colliding ^{28}Si at 35 MeV/A on a fixed ^{12}C target [28]. At the predicted energy region, a total of three sharp resonances instead of just a single resonance have been observed and interpreted as possible toroidal high-spin isomers with spins $I = I_z = 28$, 36, and 44 in the excited ^{28}Si system. Subsequent relativistic mean-field calculations provide additional theoretical support for the presence of these states [21–23]. We would like to understand in a simple mechanical way how high-spin nuclei can be produced in the binary products of such reactions. We would also like to investigate the process of punching of a small nucleus through a larger nucleus [3] for the generation of vorticities, if only heuristically.

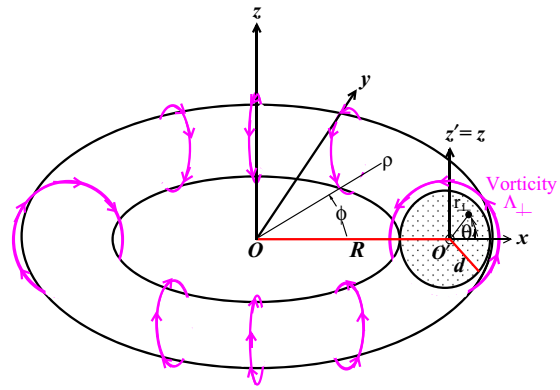

FIG. 1. The cylindrical coordinates (ρ, z, ϕ) and toroidal coordinates $(r_\perp, \theta, \phi)$ used for the description of a toroidal nucleus with a major radius R, a minor radius d, and a vorticity $\Lambda_\perp$. Here, ϕ is the toroidal angle, θ is the poloidal angle, and $r_\perp = [(\rho - R)^2 + z^2]^{1/2}$. Some of the poloidal vortex flow lines are schematically exhibited.

This paper is organized as follows: In Sec. II, we introduce the toroidal single-particle potential and evaluate the single-particle eigenenergies analytically as shown in the appendix. In Sec. III, we display the single-particle-state energies in the intermediate-mass region and infer the toroidal shell magic number N in a region of low single-particle energy densities as a function of the toroidal deformation R/d. In Sec. IV, we examine how one can carry out the spin-aligning Bohr–Mottelson particle-hole excitations to lead to toroidal high-spin isomers as yrast states in the intermediate-mass region. The set of nucleon numbers and spin quantum numbers for the favorable configurations at $R/d = 2.9$ are presented as an example. In Sec. V, we make the coordinate transformation from the Cartesian-like coordinates of $(\rho - R, z)$ to the polar coordinates $(r_\perp, \theta)$ on the meridian plane in order to exhibit explicitly the vorticity quantum number $\Lambda_\perp$. In Sec. VI, we show how we can construct a vortex nucleus by vortex-creating single-particle particle-hole excitations. In Sec. VII, we examine some experimental methods in the production of toroidal high-spin isomers and toroidal vortex nuclei. Section VIII concludes the present discussions.

II. TOROIDAL SINGLE-PARTICLE POTENTIAL

The study of the shell structure of a toroidal nucleus necessitates the use of a toroidal single-particle potential, which has a shape similar to the toroidal density distribution.

Accordingly, we assume a single-particle toroidal potential of the form [3]

$$V_0(\rho, z) = \tfrac{1}{2}m\omega_\perp^2(\rho - R)^2 + \tfrac{1}{2}m\omega_\perp^2 z^2, \tag{1}$$

where the z axis is the symmetry axis, $\rho = (x^2 + y^2)^{1/2}$ as shown in Fig. 1. The quantity m is the nucleon rest mass and $\omega_\perp$ is the harmonic-oscillator frequency related to the aspect ratio R/d by [3]

$$\hbar\omega_\perp = \left(\frac{3\pi R/d}{2}\right)^{1/3}\hbar\mathring{\omega}_0 \tag{2}$$

where

$$\hbar\mathring{\omega}_0 = 41\ \mathrm{MeV}/A^{1/3}. \tag{3}$$

The above equation for $\hbar\mathring{\omega}_0$ needs to be modified. In earlier Hartree–Fock–Bogoliubov (HFB) calculations [17], the average toroidal nuclear matter density ρ_{toroidal} is approximately 2/3 of the nuclear matter density ρ_0 of the spherical nucleus with the same mass number. Because the mean-field potential is proportional approximately to the nuclear matter density, we need to include an additional factor $\rho_{\mathrm{toroidal}}/\rho_0$ in Eq. (3) to give

$$\hbar\mathring{\omega}_0 = (41\ \mathrm{MeV}/A^{1/3})(\rho_{\mathrm{toroidal}}/\rho_0). \tag{4}$$

We have $(\rho_{\mathrm{toroidal}}/\rho_0) \sim 0.64$ for $A \sim 40$ [17], and $(\rho_{\mathrm{toroidal}}/\rho_0) \sim 1.0$ for superheavy nuclei [26], we can therefore take the average value of $(\rho_{\mathrm{toroidal}}/\rho_0) \sim 0.82$ for our intermediate-mass region of $A \sim 60$–160, where we shall use $A = 110$ in Eq. (4) for numerical purposes.

With the inclusion of the spin-orbit interaction, the single-particle potential is

$$H = -\frac{\hbar^2}{2m}\nabla^2 + V_0(\rho, z) - \frac{2\kappa\hbar}{m\mathring{\omega}_0}\boldsymbol{s}\cdot(\nabla V_0 \times \boldsymbol{p}), \tag{5}$$

where κ is a dimensionless parameter for which Nilsson gave the value of $\kappa = 0.06$ [42]. We choose the spin $\boldsymbol{s}$ to be diagonal along the symmetry z axis and neglect the small contribution from the off-diagonal spin-orbit interaction. We carry out our analytical calculations in the large-major-radius approximation in which $R \gg d$, expand ρ about R in power of $q = \rho - R$, and keep terms up to the second order in q/R. The harmonic-oscillator potential can be solved analytically as shown in the appendix. We get the single-particle energies for the single-particle state $|n_\rho n_z \Lambda_z \Omega_z\rangle$:

$$\epsilon(n_\rho n_z \Lambda_z \Omega_z) = \left(n_\rho + \frac{1}{2}\right)\hbar\omega'_\perp + \left(n_z + \frac{1}{2}\right)\hbar\omega_\perp + \frac{\hbar^2}{2m}\frac{\Lambda_z^2 - \frac{1}{4}}{R^2} + a_0, \tag{6}$$

where n_ρ and n_z are the quantum numbers for harmonic oscillations in the ρ and z directions, respectively, Λ_z is the azimuthal angular-momentum quantum number, $\Omega_z = \Lambda_z + s_z = \pm|\Omega_z|$,

$$\omega'^2_\perp = \omega_\perp^2(1 + a_2), \tag{7}$$

$$a_2 = \frac{1}{m\omega_\perp^2}\left\{\frac{\hbar^2}{2m}\frac{\Lambda_z^2 - \frac{1}{4}}{R^2}\frac{6}{R^2} + \frac{2\kappa(\hbar\omega_\perp)^2}{\hbar\mathring{\omega}_0}s_z L_z\frac{2}{R^2}\right\}, \tag{8}$$

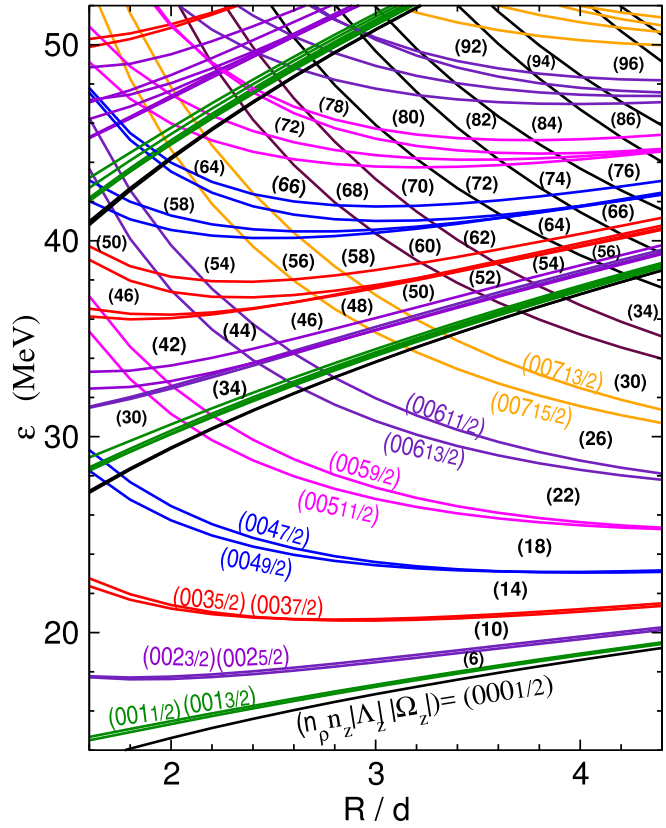

FIG. 2. Single-particle energies for a toroidal nucleus as a function of the aspect ratio R/d. The states are labeled by quantum numbers $(n_\rho, n_z, |\Lambda_z|, |\Omega_z|)$, which are displayed only for the lowest states. The locations of the toroidal shell are shown as bracketed numbers, (N), at their corresponding toroidal deformations, R/d.

$$a_0 = \frac{1}{2}m\omega_\perp^2 q_0^2 + \frac{\hbar^2}{2m}\frac{\Lambda_z^2 - \frac{1}{4}}{R^2}\left(-\frac{2q_0}{R} + \frac{3q_0^2}{R^2}\right) - \frac{2\kappa(\hbar\omega_\perp)^2}{\hbar\mathring{\omega}_0}s_z L_z\left(\frac{q_0}{R} - \frac{q_0^2}{R^2}\right), \tag{9}$$

$$q_0 = \frac{1}{m\omega_\perp^2(1 + a_2)}\left\{\frac{\hbar^2}{2m}\frac{\Lambda_z^2 - \frac{1}{4}}{R^2}\frac{2}{R} + \frac{2\kappa(\hbar\omega_\perp)^2}{\hbar\mathring{\omega}_0}\frac{s_z L_z}{R}\right\}. \tag{10}$$

III. TOROIDAL SINGLE-PARTICLE STATES

The single-particle-state energies in Eq. (6) lead to the level diagram as a function of the toroidal deformation R/d shown in Fig. 2. A toroidal shell $(N, R/d)$ is characterized by the nucleon number N, for which the single-particle states have an energy gap at the toroidal deformation R/d. We indicate the location of a toroidal shell $(N, R/d)$ by a bracketed number (N) at its corresponding toroidal deformation R/d in Fig. 2.

We find that toroidal shells are numerous in number in light- and intermediate-mass nuclei. As the nucleon number increases beyond the light-mass region, nucleons populate states with $n = n_\rho + n_z \geqslant 1$ and the density of single-particle

TABLE I. Locations of toroidal shells in the intermediate-mass region.

Toroidal deformation R/d	Toroidal shell nucleon numbers (N)
∼1.8	(30), (42), (46), (50)
∼2.2	(34), (44), (54), (58),(64)
∼2.5	(46), (56), (66), (72)
∼2.9	(48), (58), (68), (78)
∼3.2	(50), (60), (70), (80)
∼3.5	(52), (62), (72), (82), (92)
∼3.8	(54), (64), (74), (84), (94)
∼4.2	(56), (66), (76), (86), (96)

states initially becomes very dense. The density, however, becomes sparse as the nucleon number and toroidal deformation increase. As indicated in Fig. 2, large energy gaps of single-particle energy levels occur to give rise to toroidal shells for many nucleon numbers at various toroidal deformations. The toroidal shells (N, R/d) in the intermediate-mass region with $30 \lesssim N$ (or Z) $\lesssim 96$ are listed in Table I.

We note that the toroidal shells occur in a rather regular pattern as a result of the interplay among three different energies scales, as is evident from Eq. (6). There is first of all the gross structure energy scale of $\hbar\omega_\perp$ of order 10 MeV that increases with R/d. There is the much smaller energy scale of $\hbar^2/2mR^2$ of order 1 MeV with single-particle orbiting energies $\Lambda_z^2\hbar^2/2mR^2$. And, finally, there is the small finer-structure arising from the spin-orbit interactions. As a result of the interplay between these three energy scales, we note the following regular structure:

(1) As a function of increasing toroidal deformation R/d, there are sequences of toroidal shells occurring at an interval of $\Delta(R/d) \sim 0.3$ and $\Delta N = 2$.
(2) For a fixed value of toroidal deformation R/d, there are sequences of toroidal shells occurring at an interval of $\Delta N = 10$ arising from nucleons occupying four ($n_\rho + n_z = 1$, Λ_z) states and a single ($n_\rho + n_z = 0$, Λ_z') state.

There are toroidal shells with nucleon numbers (30), (42), (46), and (50) at $R/d \sim 1.8$, $(34 + 10m)$ and (58) at $R/d \sim 2.2$, $(46 + 10m)$ and (72) at $R/d \sim 2.4$, $(48 + 10m)$ at $R/d \sim 2.9$, $(50 + 10m)$ at $R/d \sim 3.2$, $(52 + 10m)$ at $R/d \sim 3.5$, $(54 + 10m)$ at $R/d \sim 3.8$, and $(56 + 10m)$ at $R/d \sim 4.2$. The integer m in these toroidal shell series starts with $m = 0$ and terminates with $m = 3$, or 4, until the $n = n_\rho + n_z = 2$ single-particle states are reached.

Nuclei with toroidal shells gain extra stability at the associated toroidal deformation. Consequently, they present themselves as good candidates in the search for excited toroidal local energy minima in microscopic model calculations, as carried out in previous Strutinsky shell correction calculations or in self-consistent mean-field calculations [2,3,14,28].

It is interesting to note that, in the intermediate-mass region, many toroidal shells of different nucleon numbers occur at approximately the same toroidal deformation. This feature facilitates the combinations of different neutron and proton numbers to maximize the shell effects at the same toroidal deformation and at the same time minimize the instability against beta decay. However, because of the Coulomb interaction, the proton toroidal shell nucleon number and toroidal deformations will be slightly modified from those listed in Table I. The repulsive single-particle proton potential is greatest near the region of the greatest nuclear densities and therefore the single-particle Coulomb potential behaves approximately as an inverted harmonic oscillator in the meridian plane. To the lowest order of modification, it will effectively modify the harmonic-oscillator frequency $\hbar\omega_\perp$ so that one effectively speaks of $\hbar\omega_\perp$(neutron) for the neutron and a slightly modified $\hbar\omega_\perp$(proton) for the proton. We expect from Eq. (6) that, similar to the neutron toroidal shells there will likewise be proton toroidal shells at various toroidal deformations. Furthermore, because of the regularity of the shell structure and the frequent occurrences of the toroidal shells in both nucleon numbers and toroidal deformations, one expects that there will be many combinations of proton and neutron toroidal shells occurring at the same toroidal deformation to make them favorable for the stabilization due to the nuclear-shell effects. Future microscopic models will provide a better description of the toroidal nuclei possibilities in the intermediate-mass region.

IV. TOROIDAL HIGH-SPIN ISOMERS IN INTERMEDIATE-MASS REGION

In addition to the toroidal shell structure characterized by the nucleon number N at the toroidal deformation R/d, there is the spin degree of freedom that is worth exploring for the intermediate-mass region. Relative to an even-even core of a toroidal nucleus occupying the lowest toroidal single-particle states at a given toroidal deformation R/d, toroidal high-spin isomers with different spins as yrast states may be constructed with the spin-aligning Bohr–Mottelson particle-hole excitations [41] as carried out in Refs. [15–20,25–27]. The $I = 0$ toroidal core nucleus may be in a local energy minimum, if the nucleus has both neutron and proton toroidal shells and the associated shell correction energy is strong enough to allow an energy minimum [28]. On the other hand, if the shell correction is not strong enough to allow an energy minimum or, if the nucleon numbers at that toroidal deformation fall into regions of high single-particle state density with positive shell corrections, then the toroidal nucleus will be away from a local energy minimum [25–27]. In either case, high-spin toroidal isomers can nevertheless be constructed from the $I = 0$ toroidal core by using the spin-aligning Bohr–Mottelson particle-hole excitations [41] by promoting nucleons occupying states with an angular momentum opposite to a chosen symmetry axis to occupy empty states with an angular momentum along the symmetry axis.

Using the cranking frequency $\hbar\omega$ as a Lagrange multiplier, the particle-hole excitation leading to a particular angular momentum yrast $I = I_z$ state can be obtained by occupying the lowest Routhian single-particle orbitals as a function of $\hbar\omega$, as was shown in previous cranked self-consistent Hartree–Fock calculations [15–20,25–27]. The single-particle

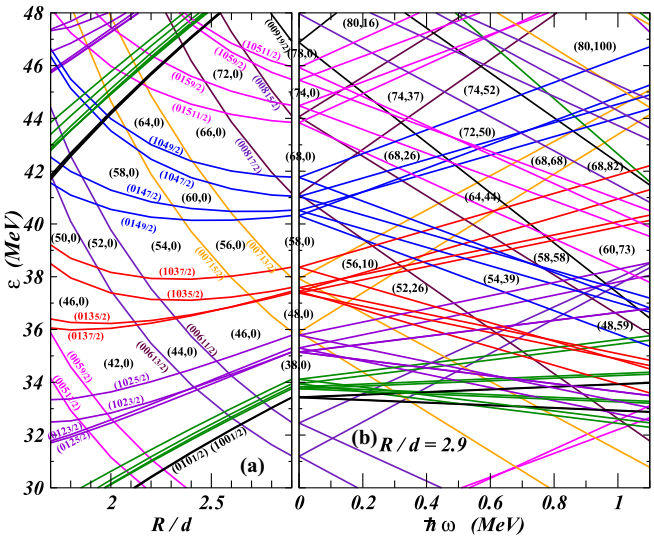

FIG. 3. (a) Single-particle state energy ϵ for a toroidal nucleus as a function of the aspect ratio R/d. The states are labeled with quantum numbers $(n_\rho, n_z, |\Lambda_z|, |\Omega_z|)$. (b) Single-particle Routhian $\epsilon_{\rm Routhian}$ as a function of the cranking frequency $\hbar\omega$, at the toroidal deformation $R/d = 2.9$. The bracketed numbers are favorable (N, I) configurations at this deformation.

Routhian $\epsilon_{\rm Routhian}(n_\rho n_z \Lambda_z \Omega_z)$, under the constraint of the noncollective aligned angular momentum is related to the single-particle energy $\epsilon(n_\rho n_z \Lambda_z \Omega_z)$ by

$$\epsilon_{\rm Routhian}(n_\rho n_z \Lambda_z \Omega_z) = \epsilon(n_\rho n_z \Lambda_z \Omega_z) - \hbar\omega \Omega_z. \qquad (11)$$

It is necessary to investigate the shell structure in the space of N, R/d, and $\hbar\omega$. As an example, we show the shell structure at $R/d = 2.9$ where many toroidal shells are located. It is of interest to see how different toroidal shell structure evolve as a function of the cranking frequency $\hbar\omega$. We show in Fig. 3 the multidimensional nature of the shell structure by exhibiting the single-particle state energy as a function of R/d in Fig. 3(a), and the the single-particle Routhian energy as a function of $\hbar\omega$ at $R/d = 2.9$ in Fig. 3(b). We can use Fig. 3(b) to determine the spin value $I = I_z$ as a function of N and $\hbar\omega$ at $R/d = 2.9$. Specifically, for a given N and $\hbar\omega$, the aligned $I = I_z$ from the N nucleons occupying the lowest Routhian energy states can be obtained by summing Ω_{zi} over all states below the Fermi energy and the summed aligned angular momentum I is a step-wise function of the Lagrange multiplier $\hbar\omega$ [43], with each I spanning a small region of $\hbar\omega$. By such a construction, we obtain selective regions of low Routhian energy level densities at different $(N, I, R/d)$ configurations at the top of the Fermi energy and the toroidal deformation R/d. These $(N, I, R/d)$ configurations are favorable candidates in search of toroidal high-spin isomers [17] in microscopic models. We show the locations of favorable (N, I) configurations for $R/d = 2.9$ in Fig. 3(b).

It is interesting to note in Fig. 3(b) that, at $R/d = 2.9$ and $\hbar\omega \sim 0.4$ MeV, the shell regions of low Routhian energy level density occur for $(N, I) = (52, 26)$, (68,26), and (74,37) which may allow various $(Z, I_{\rm proton})$ and $(N, I_{\rm neutron})$ combinations to be good candidates for toroidal high-spin isomers. At $\hbar\omega \sim 0.6$ MeV, the shell regions of low Routhian density occur for (54,39), (64,44), (72,50), and (74,52). At $\hbar\omega \sim 0.8$ MeV, the shell regions of low Routhian density occur for (58,58) and (68,68), and at $\hbar\omega \sim 1.0$ MeV they occur at (48,59), (68,73), (68,82), and (80,100). Note that there are many nucleon numbers (such as $N = 52$, 74, 80, 54, 64, …) in these favorable configurations that are not toroidal shell numbers associated with extra stability at $\hbar\omega = 0$ without cranking at $R/d = 2.9$. These nucleon numbers nevertheless may be favorable for high-spin isomers because of their shell structure as a function of $\hbar\omega$ under a cranking motion, as in the analogous case in the superheavy nuclei region [26]. From this viewpoint, it is not always necessary to have a toroidal core located at an energy minimum to make the Bohr–Mottelson spin-aligning single-particle excitations for toroidal high-spin isomers. What is necessary is the low Routhian energy density under the cranking motion that provides the favorable condition to stabilize toroidal high-spin isomers. Favorable (N, I) configurations occur at other toroidal deformations R/d as well.

The results in Fig. 3 demonstrate that, just as it is with light-mass nuclei, toroidal high-spin isomers are also expected in the intermediate-mass region. The shell structure is, however, a very complicated function of toroidal deformation and the cranked frequency. Thus the occurrence of the favorable combination shell region $(N, I, R/d)$ for toroidal isomers can only be treated on a case-by-case basis. The search for high-spin isomers can proceed as in Refs. [14,17–20,25–27] by using figures similar to Fig. 3 as a guide.

The spin and the excitation energy of a toroidal high-spin isomer can be calculated in the self-consistent mean-field theory. It can also be estimated in the toroidal shell model as was carried out in Ref. [28]. In such an estimate, upon promoting a nucleon from an initial orbital $(n_\rho, n_z, \Lambda_z, \Omega_z)_i$ to become a hole state and to occupy an empty final orbital $(n_\rho, n_z, \Lambda_z, \Omega_z)_f$, one calculated the change in the aligned angular momentum and the excitation energy for such a promotion from the quantum numbers and the single-particle energies of the particle-hole states. The total spin $I = I_z$ and total excitation energy $E_I - E_{I=0}$ are then the sums from all particle-hole promotions. The spin of the toroidal nucleus is given by

$$I_z = \sum_f^{\text{particle states}} \Omega_{zf} - \sum_i^{\text{hole states}} \Omega_{zi}, \qquad (12)$$

and the total excitation energy is given by

$$E_I - E_{I=0} = \sum_f^{\text{particle states}} \epsilon(n_\rho n_z \Lambda_z \Omega_z)_f - \sum_i^{\text{hole states}} \epsilon(n_\rho n_z \Lambda_z \Omega_z)_i. \qquad (13)$$

It should, however, be stressed that what has been presented here with the analytical toroidal single-particle shell model provides only an intuitive guide on the interesting nuclei where toroidal high-spin isomers may be searched and located. Whether these states turn out to be local energy minima will need to rely on reliable microscopic models

TABLE II. The equivalence of $(n_\rho, n_z) \to (n_\perp, \Lambda_\perp)$ for the toroidal single-particle states.

$n_\rho + n_z$	$(n_\rho n_z)$ states	$(n_\perp, \Lambda_\perp)$ states	Number of states
0	(0, 0)	(0,0)	1
1	(0,1) (1,0)	(0, +1) (0, −1)	2
2	(0,2), (2,0), (1,1)	(0, +2), (0, −2), (1,0)	3
3	(0,3), (3,0), (1,2), (2,1)	(0,3), (0, −3), (1,1), (1, −1)	4

such as the nonrelativistic mean-field or relativistic mean-field calculations as carried out in Refs. [11–29].

V. TOROIDAL NUCLEI WITH VORTICITIES

The geometrical shape of a toroidal nucleus provides a natural way to describe nuclear vorticities, as shown in Fig. 10 of Ref. [3] and in Fig. 1. The concept of vortex nucleus is best examined in the limit of a toroidal nucleus with a large major radius R so that we can neglect d/R, and the difference between $\hbar\omega_\perp$ and $\hbar\omega'_\perp$ is small and can be neglected. Within this approximation, we can rewrite Eqs. (A13) and (A7) as

$$\left[-\frac{\hbar^2}{2m}\left(\frac{\partial^2}{\partial q^2} - \frac{\Lambda_z^2 - \frac{1}{4}}{R^2}\right) - \frac{\hbar^2}{2m}\frac{\partial^2}{\partial z^2} + \frac{1}{2}m\omega_\perp^2 q^2 + \frac{1}{2}m\omega_\perp^2 z^2 - \frac{2\kappa\hbar}{m\mathring{\omega}_0}\frac{m\omega_\perp^2}{R/d}s_z\Lambda_z - \epsilon(n_\rho n_z\Lambda_z\Omega_z)\right]\mathcal{R}_{n_\rho}(\rho)Z_{n_z}(z) = 0. \tag{14}$$

where $q = \rho - R$. We can transform the two-dimensional (q, z) coordinates to polar coordinates $(r_\perp, \theta)$ where

$$r_\perp = \sqrt{q^2 + z^2}, \quad \theta = \tan^{-1}(z/q), \tag{15}$$

and θ is the poloidal angle as shown in Fig. 1. We can rewrite Eq. (14) as

$$\left[-\frac{\hbar^2}{2m}\left(\frac{1}{r_\perp}\frac{\partial}{\partial r_\perp}r_\perp\frac{\partial}{\partial r_\perp} - \frac{\Lambda_\perp^2}{r_\perp^2}\right) + \frac{1}{2}m\omega_\perp^2 r_\perp^2 + \frac{\hbar^2\left(\Lambda_z^2 - \frac{1}{4}\right)}{2mR^2} - \frac{2\kappa\hbar}{m\mathring{\omega}_0}\frac{m\omega_\perp^2}{R/d}s_z\Lambda_z - \epsilon(n_\perp\Lambda_\perp\Lambda_z\Omega_z)\right]\Re_{n_\perp\Lambda_\perp}(r_\perp)e^{i\Lambda_\perp\theta} = 0. \tag{16}$$

In Eq. (14), the two-dimensional harmonic-oscillator nucleon wave function $\mathcal{R}_{n_\rho}(\rho)Z_{n_z}(z)$ in (q, z) coordinates in the meridian plane with quantum numbers (n_ρ, n_z) has been transformed into $\Re_{n_\rho\Lambda_\perp}(r_\perp)e^{i\Lambda_\perp\theta}$ in $(r_\perp, \theta)$ coordinates with quantum numbers $(n_\perp, \Lambda_\perp)$ in the above equation. Note that the wave function $e^{i\Lambda_\perp\theta}$ describes the state with vorticity $\Lambda_\perp$ associated with a circulating vortex current around the poloidal angle θ in the meridian plane, as shown in Fig. 1. It is the poloidal angular momentum along the poloidal angular direction. If only a single $e^{i\Lambda_\perp\theta}$ state is occupied, we have a state of vorticity $\Lambda_\perp$, but if there is a pair of nucleons occupying both $\pm|\Lambda_\perp|$ states, then the vorticities of these two nucleons cancel each other, and we have a state of zero total vorticity. If by construction when there is a bias in occupying more positive $\Lambda_\perp$ states than negative $\Lambda_\perp$ states (or vice versa), then there will be a net nonzero $\Lambda_\perp$ and consequently a net nonzero total vorticity.

The two-dimensional harmonic-oscillator energy in $(n_\rho n_z)$ and in $(n_\perp\Lambda_\perp)$ are related by

$$(n_z + n_\rho + 1)\hbar\omega_\perp = (2n_\perp + |\Lambda_\perp| + 1)\hbar\omega_\perp. \tag{17}$$

We have the equivalence between the toroidal states in $(n_z n_\rho)$ and in $(n_\perp\Lambda_\perp)$ in Table II which shows that a nucleon in a toroidal nucleus residing at states with $n_z + n_\rho \geqslant 1$ possesses a nonzero vorticity quantum number $\Lambda_\perp$. We can relabel the set of states with quantum numbers $(n_\rho n_z)$ to $(n_\perp\Lambda)$,

$$|n_\rho n_z\Lambda_z\Omega_z\rangle \to |n_\perp\Lambda_\perp\Lambda_z\Omega_z\rangle. \tag{18}$$

Clearly, the $\Lambda_\perp = \pm|\Lambda_\perp|$ states are degenerate. Vorticity is a new degree of freedom not available for light nuclei studied in Refs. [14–20,28].

The single-particle energy of $|n_\perp\Lambda_\perp\Lambda_z\Omega_z\rangle$ is therefore given from Eq. (16) by

$$\epsilon(n_\perp\Lambda_\perp\Lambda_z\Omega_z) = (2n_\perp + |\Lambda_\perp| + 1)\hbar\omega_\perp + \frac{\hbar^2\left(\Lambda_z^2 - 1/4\right)}{2mR^2} - \frac{2\kappa\hbar}{m\mathring{\omega}_0}\frac{m\omega_\perp^2}{R/d}s_z\Lambda_z. \tag{19}$$

The vorticity of a nucleus or a nucleon is a quantized quantity and is measured in units of $\hbar$. After the symmetry z axis has been chosen, as for example as the axis pointing in the upward direction in Fig. 1, then we can designate the vorticity to be positive by the right handedness of the poloidal flow on the right rim of the nucleus, according to the sense of the poloidal angle θ, as shown in Fig. 1 between the ρ axis and the radial vector $\mathbf{r}_\perp$. Negative vorticity corresponds to the case of left handedness of the poloidal flow. The handedness property of the poloidal flows allows one to associate the vorticity quantum numbers also with equivalent chirality quantum numbers, with positive and negative vorticities associated with positive and negative chiralities, respectively. Clearly, if the toroidal vortex nucleus has a nonzero spin about the symmetry axis, the toroidal vortex nucleus with opposite vorticities (or chiralities) are distinguishable physical states.

Vorticity is a good quantum number and it is a conserved quantity. It would be of interest to study the production the decay of these nuclei to see if they may show up as exotic metastable states with a toroidal topology and flow patterns.

VI. HOW TO CONSTRUCT A VORTEX NUCLEUS

We can use Table II to construct a nucleus with a total vorticity $\Lambda_\perp^{\text{total}}$. The vorticity quantum number of a nucleon

TABLE III. The configurations of the eight topmost occupied single-particle states at the top of the Fermi energy for $Z = 48$ and $R/d = 2.9$ in Fig. 2. In this configuration, the total proton vorticity for this state, $\Lambda_{\perp\text{proton}}^{\text{total}}$, and the total spin Ω_z^{total} are zero.

$n_\perp$	Vorticity $\Lambda_\perp$	$\lvert\Lambda_z\rvert$	Ω_z
0	1	2	3/2
0	−1	2	3/2
0	1	2	−3/2
0	−1	2	−3/2
0	1	2	5/2
0	−1	2	5/2
0	1	2	−5/2
0	−1	2	−5/2

$\Lambda_\perp$ can be both positive and negative and the total vorticity $\Lambda_\perp^{\text{total}}$ for an N (or Z) nucleon system is the sum of the vorticities of its constituent nucleons, $\Lambda_{\perp i}$:

$$\Lambda_\perp^{\text{total}} = \sum_i^{N\ (\text{or}\ Z)} \Lambda_{\perp i}. \tag{20}$$

We study a concrete example and focus our attention on the toroidal nucleus with $Z = 48$ and $N = 58$ at $R/d = 2.9$ whose large single-particle energy gaps in Fig. 2 make it likely to have an excited toroidal energy minimum stable against expansion and contraction of the major radius at that toroidal deformation. We examine first the vorticities and the energy for protons with $Z = 48$ in Tables III, IV, and Fig. 2. By populating the lowest single-particle states at this possible toroidal energy minimum, the eight topmost occupied states are $(n_\perp, \Lambda_\perp, |\Lambda_z|, \Omega_z) = (0, \pm 1, 2, (\pm 3/2))$ and $(0, \pm 1, 2, (\pm 5/2))$, each of which is degenerate with $\Lambda_z = \pm|\Lambda_z|$, $\Omega_z = \pm|\Omega_z|$. So, we have $\epsilon(n_\perp, \Lambda_\perp, |\Lambda_z|, \Omega_z) = \epsilon(0, 1, 2, (+3/2)) = \epsilon(0, 1, 2, (-3/2))$, and $\epsilon(n_\perp, \Lambda_\perp, |\Lambda_z|, \Omega_z) = \epsilon(0, 1, 2, (+5/2)) = \epsilon(0, 1, 2, (-5/2))$. Each of these four states, $(n_\perp, |\Lambda_\perp|, |\Lambda_z|, \Omega_z) = \{(0, 1, 2, (+3/2)), (0, 1, 2, (-3/2)), (0, 1, 2, (+5/2)), (0, 1, 2, (-5/2))\}$ are doubly degenerate with $\Lambda_\perp = \pm|\Lambda_\perp|$. For the configuration in which the eight topmost occupied states for $Z = 48$ are given in Table III, the total vorticity $\Lambda_\perp^{\text{total}}$ and the total spin about the z axis Ω_z^{total} are zero.

Now suppose we promote all four proton states in Table III with $\Lambda_\perp = -1$ from such $\Lambda_\perp = -1$ states to the next unoccupied level with $\Lambda_\perp = +1$ by particle-hole excitations. According to Fig. 2, the next unoccupied levels are $(n_\perp, \Lambda_\perp, |\Lambda_z|, \Omega_z) = (0, \Lambda_\perp = +1, |\Lambda_z| = 3, |\Omega_z| = 5/2\ \&\ 7/2)$. We obtain the set of occupied states in Table IV, with the promoted particle states in bracketed numbers.

The excitation energy of this $4p$-$4h$ state with eight units of vorticity from Tables III and IV in promoting the set of $\{i\}$ nucleons from the $|n_\perp \Lambda_\perp \Lambda_z \Omega_z\rangle$ states to the $|n'_\perp \Lambda'_\perp \Lambda'_z \Omega'_z\rangle$ states is

$$\begin{aligned} &E^{\text{proton}}_{\Lambda_\perp=8} - E^{\text{proton}}_{\Lambda_\perp=0} \\ &= \sum_{\text{all } i} (\epsilon_{n'_\perp \Lambda'_\perp \Lambda'_z \Omega'_z}(i) - \epsilon_{n_\perp \Lambda_\perp \Lambda_z \Omega_z}(i)) \\ &= [\epsilon(0,1,3,5/2) + \epsilon(0,1,3,-5/2) \\ &\quad + \epsilon(0,1,3,7/2) + \epsilon(0,1,3,-7/2)] \\ &\quad - [\epsilon(0,1,2,3/2) + \epsilon(0,1,2,-3/2) \\ &\quad + \epsilon(0,1,2,5/2) + \epsilon(0,1,2,-5/2)], \end{aligned} \tag{21}$$

which can be obtained from the eigenvalue equation (19). Assuming negligible spin-orbit interaction, which is probably small, we have from the protons with $Z = 48$ at $R/d = 2.9$ with a total proton vorticity $\Lambda_{\perp\text{proton}}^{\text{total}} = 8\hbar$,

$$\begin{aligned} E^{\text{proton}}_{\Lambda_\perp=8} - E^{\text{proton}}_{\Lambda_\perp=0} &= 4\frac{\hbar^2\left(\Lambda_z'^2 - \Lambda_z^2\right)}{2mR^2} \\ &= 4\frac{\hbar^2(3^2 - 2^2)}{2mR^2} = \frac{20\hbar^2}{2mR^2}. \end{aligned} \tag{22}$$

We turn now to the vorticities and the energy for neutrons with $N = 58$ at $R/d = 2.9$ in Fig. 2. Procedures similar to those given above lead to Table V, a total neutron vorticity $\Lambda_{\perp\text{proton}}^{\text{total}} = 8\hbar$, and an excitation energy

$$\begin{aligned} E^{\text{neutron}}_{\Lambda_\perp=8} - E^{\text{neutron}}_{\Lambda_\perp=0} &= 4\frac{\hbar^2\left(\Lambda_z'^2 - \Lambda_z^2\right)}{2mR^2} \\ &= 4\frac{\hbar^2(4^2 - 3^2)}{2mR^2} = \frac{28\hbar^2}{2mR^2}. \end{aligned} \tag{23}$$

TABLE IV. The configurations of the eight topmost occupied states for $Z = 48$ at $R/d = 2.9$ in Fig. 2 after the vortex-creating $4p$-$4h$ excitations with the promoted particle configurations shown in bracketed numbers. In this configuration, the total proton vorticity is $\Lambda_{\perp\text{proton}}^{\text{total}} = 8\hbar$ and $\Omega_{z\ \text{proton}}^{\text{total}} = 0$.

$n_\perp$	Vorticity $\Lambda_\perp$	$\lvert\Lambda_z\rvert$	Ω_z
0	1	2	3/2
0	(1)	(3)	(5/2)
0	1	2	−3/2
0	(1)	(3)	(−5/2)
0	1	2	5/2
0	(1)	(3)	(7/2)
0	1	2	−5/2
0	(1)	(3)	(−7/2)

TABLE V. The configurations of the eight topmost states with different state quantum numbers at the top of the Fermi energy for $N = 58$ and $R/d = 2.9$ in Fig. 2, after the vortex-creating $4p$-$4h$ excitation with the particle configuration shown in bracketed numbers. The total vorticity for this $N = 58$ state is $\Lambda_{\perp\text{neutron}}^{\text{total}} = 8\hbar$ and $\Omega_{z\ \text{neutron}}^{\text{total}} = 0$.

$n_\perp$	Vorticity $\Lambda_\perp$	$\lvert\Lambda_z\rvert$	Ω_z
0	1	3	5/2
0	(1)	(4)	(7/2)
0	1	3	−5/2
0	(1)	(4)	(−7/2)
0	1	3	7/2
0	(1)	(4)	(9/2)
0	1	3	−7/2
0	(1)	(4)	(−9/2)

The total excitation energy of $(Z, N) = (48, 58)$ with a total vorticity of $16\hbar$ is

$$E_{\Lambda_\perp=16} - E_{\Lambda_\perp=0} = \frac{48\hbar^2}{2mR^2}, \tag{24}$$

which decreases as R/d increases. Here the number 4 on the right-hand sides of Eqs. (22) and (23) is the number N_{ph} of particle-hole excitations that promote the negative $\Lambda_\perp = -1$ to the positive $\Lambda_\perp = +1$ states (or vice versa) and can be changed to get a state with a different vorticity. Thus, the greater the number of particle-hole promotion N_{ph}, the greater is the vorticity, and the greater is the effect on lowering the energy of the system by moving to greater R values. In other words, there is an energy associated with a given vorticity and, for a given vorticity, the larger the R, the lower the energy of the system. The toroidal system likes to expand to a greater radius R, if the nucleus has a vorticity.

In the above example, we have made a $4p$-$4h$ excitation to obtain an excited state of vorticity $\Lambda_\perp(\text{neutron}) = \Lambda_\perp(\text{proton}) = 8\hbar$. It is possible to make np-nh excitations with $n = 1$ to 4 for both neutrons and protons, with the only modification that the total Ω_z would vary according to the Ω_z value of the particle-hole configuration. The signature of the vorticity occurrence is therefore a set of states with vorticity $\Lambda_\perp = 2, 4, 6, 8, \ldots$, and 16, with about equal energy spacing.

What we have presented is an example of how we can construct a toroidal vortex nuclei with different vorticities for $Z = 48$ and $N = 58$ at $R/d = 2.9$. Other toroidal vortex nucleus can be similarly constructed for different neutron and proton numbers at various toroidal deformations. The large number of toroidal shells as listed in Table I provide a large pool of neutron and proton combinations for which toroidal vortex nuclei may be constructed at different toroidal deformations. Therefore, there can be many different toroidal vortex nuclei with different neutron and proton numbers constructed by making vortex-creating particle-hole single-particle excitations in the intermediate-mass region. The possibility for nucleons possessing a nonzero vortex quantum number with $n = n_\rho + n_z > 1$ in the heavy-mass region implies that toroidal vortex nuclei are also expected in the heavy-mass region.

VII. POSSIBLE MECHANISMS FOR THE PRODUCTION OF TOROIDAL HIGH-SPIN ISOMERS AND TOROIDAL VORTEX ISOMERS

The method of production and detection of toroidal nuclei depends on their lifetimes which are however difficult to estimate because they require the knowledge of the potential-energy surface and the effective-mass parameter in many different degrees of freedom. Many mean-field calculations from independent groups have been carried out [11–20,25–29]. They indicate stability against small-amplitude oscillations, as three-dimensional calculations with three-dimensional noises have been carried out and they yield toroidal high-spin isomeric energy minima. However, the stability against large-amplitude oscillations, as for example against the Plateau–Rayleigh instability [44–46], is not known. Subject to further studies to confirm or refute the experimental evidence for possible population of toroidal high-spin isomers in Ref. [28], the tentative extraction of the width for toroidal ^{28}Si high-spin isomer indicates that the widths may be broad for low-spin states, become narrower than the instrument bin size of 3 to 4 MeV for the $I = 28$, 36, and 44 states, and they become broader again for possible higher-spin states. We may expect that the lifetime depends on the spins and the excitation energies. For low-spin states, as they lie in highly excited region of states of similar angular momentum from the co-existing sphere-like geometry, there may be extensive mixing that will likely broaden the widths and shorten the lifetimes of these low-spin states. Longer lifetimes may be reached by promoting nucleons to populate higher but well-bound single-particle orbitals to lead to higher-spin toroidal high-spin isomers as yrast states with hardly any mixing of states of similar angular momentum from the sphere-like geometry. However, when the nucleons are promoted to higher-energy orbitals that may be above or near the nucleon drip line in higher excitation energies, the widths of these high-spin states may be broadened again, with shorter lifetimes.

A. Production of light-mass toroidal isomers by elastic scattering

In recent years, time projection chambers (TPCs) have been used to study the nuclear spectroscopy of metastable nuclei [47–51]. The idea is to use a chamber of noble gas under a high voltage so that the gas itself or an embedded solid layer serves as the target, and the nuclear trajectories show up as tracks. The production of a composite nucleus with a long half-life would show up as a single track with the mass and charge arising from the fusion of the projectile and target nuclei. The production of binary products indicates a two $\rightarrow$ two reaction from which one can examine the elastic and inelastic channels and study the excitation function and angular distribution to search for various metastable states. Previously, many metastable states formed by colliding various projectile nuclei with an active He target have been found by such a technique [47]. We can search for toroidal high-spin isomers as resonances or metastable nuclei by bombarding projectile nucleus on an active-target nucleus such as ^{20}Ne, ^{36,38,40}Ar, or ^{80,82,83,84,86}Kr, or ^{28}Si.

B. Production of a toroidal high-spin isomer by deep-inelastic scattering

In a deep-inelastic collision between two heavy-ions at an energy near the Fermi energy, there are reaction products consisting of highly excited binary systems with large angular momenta, in regions that may be kinematically separable [30–39]. This led Cao *et al.* [28] to suggest the use of such deep-inelastic collisions for the production of light toroidal high-spin isomers.

We present below a schematic description how the deep-inelastic collision mechanism may lead to a toroidal high-spin isomer, if (E, I) is appropriately the same as that of the toroidal high-spin isomer. We envisage that, in a deep-inelastic scattering in the target rest frame in Fig. 4, the semiperipheral collision allows the spectator nucleons of the projectile to stream forward, while the participant projectile

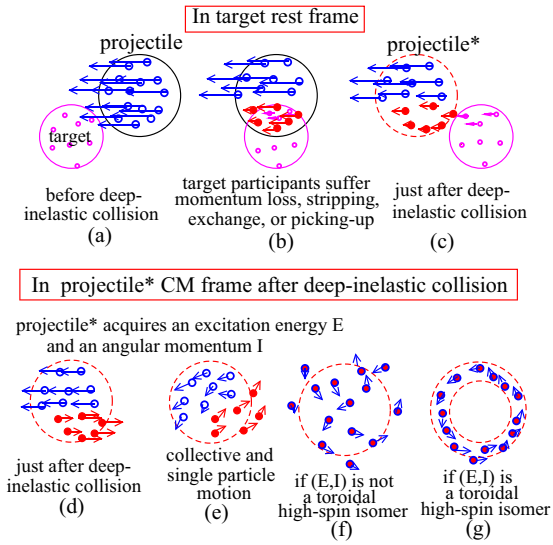

FIG. 4. A schematic example of how a toroidal high-spin isomer of an excited projectile may be produced by a deep-inelastic heavy-ion scattering between a projectile nucleus and a target nucleus, showing a cut in the collision plane. We display (a)–(c) in the target nucleus rest frame, and we show (d)–(g) in the excited projectile frame. The time sequence proceeds from (a) to (e). How (e) evolves to (f) or (g) depends on whether the excitation energy E and spin $I = I_z$ are the same as those of the toroidal high-spin isomers.

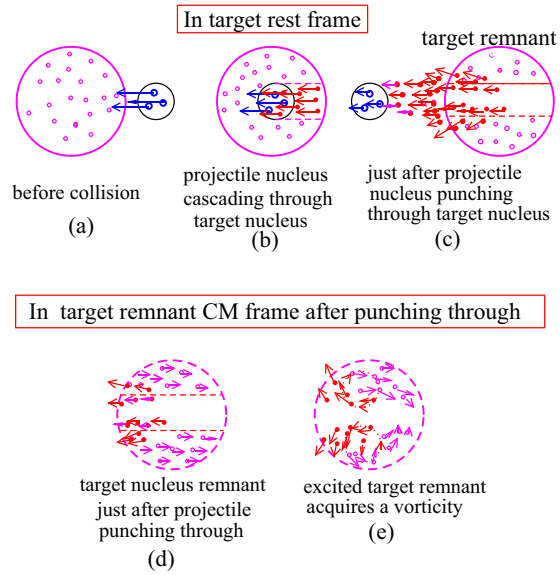

FIG. 5. A schematic example of how a toroidal vortex isomer of the excited target remnant may be produced by the punching through of a smaller projectile on a larger target nucleus in an energetic nearly-head-on collision, showing a cut in the collision plane. We display (a)–(c) in the target nucleus rest frame, while we show (d)–(e) in the excited remnant center-of-mass frame.

nucleons collide with target nucleons and suffer a deceleration, as is depicted in Figs. 4(a)–4(c). As a consequence, the excited projectile nucleus that emerges after the deep-inelastic collision is a spinning nucleus in its own center-of-mass frame. It acquires both a collective cranking motion and particle-hole excitations at an excitation energy E and an angular momentum I. Its evolution can be schematically depicted as in Figs. 4(d)–4(g). When the excitation energy E and the angular momentum I of the emerging excited projectile are not those of a toroidal isomer, the excited projectile nucleus will break up as described in statistical models [35–39]. On the other hand, when the excitation energy E and the angular momentum I of the emerging projectile corresponds to that of a toroidal high-spin isomer, the collective cranking motion and the rearrangement of the single-particle motion of the nucleons may eventually settle down into the toroidal shape of the high-spin isomer self-consistently because of the conservation of energy and angular momentum, and the many-body final-state interactions.

C. Production of a toroidal vortex nucleus by punching through a target nucleus

It has been suggested that a toroidal nucleus may be produced by punching an energetic smaller heavy ion nearly head on through a larger target nucleus [3]. Scattering and evaporation takes place within a small cone of the incident ion. The "remnant" after prompt cascade and evaporation may have a hole in the middle and consequently have the geometry of a torus, as depicted in Fig. 5. After the incident projectile ion has punched through the target nucleus, the target nucleons in the interaction regions receive a momentum kick and have a velocity different from that of the spectator target nucleons. In the center-of-mass system of the target remnant nucleus, vorticity will be developed as depicted in Fig. 5. Indeed, vorticity has been found theoretically in the hydrodynamical and model calculations in the collision of high-energy heavy ions [52–55]. Vorticity in heavy-ion collisions reveal two vortical structures that are common in many fluid dynamic systems. The vorticity and pairing of longitudinal vortices with opposite signs are generated in the transverse plane. The punching through of a large nucleus to form a toroidal nucleus [3] may therefore be a promising mechanism for the generating isolated toroidal vortex nuclei.

In addition to using energetic small heavy-ions to punch through a target nucleus one can also use the collision of an antineutron or antiproton to punch through the target nucleus for the production of a toroidal nucleus with a vorticity. We envisage that, at appropriate collision energies, annihilation of the antiparticle takes place inside the nucleus, and the momentum of the incident high-energy antiparticle carries the produced particle forward in the form of a cone, with the possibility of creating a hole inside the target nucleus. Among the remnants from such a collision, some target nucleons receive a momentum kick from the produced particles and a toroidal nucleus with vorticity may be created in a way similar to what is depicted in Fig. 5.

Toroidal galaxies (ring galaxies) have been known for some time [56–60]. It is generally held that many of these ring galaxies arise from the collision of two galaxies, and the catalog of Ref. [59] list 127 observed ring collision galaxies. The most well-known example is Arp147, which is composed of newly formed bright stars arising from the collision of one smaller galaxy through another larger galaxy. When the

two galaxies collided, they pass though each other and the gravitational wave from the impact leads to the condensation of the gas and dust into stars [60]. The observations of the ultraluminous x-ray sources in the ring galaxy Arp147 in a ring of beads confirm the conventional wisdom that collisions of gas-rich galaxies trigger large rates of star formation which, in turn, generate substantial numbers of x-ray sources, some of which have luminosities above the Eddington limit for accreting stellar-mass black holes as ultraluminous x-ray sources [60]. Another example is Arp148 showing a ring with a jet of a smaller galaxy along the symmetry axis of the ring [57]. The existence of toroidal galaxies is only suggestive that, if a toroidal vortex nucleus could be formed in the collision of a light nucleus with a heavy nucleus in a nearly-head-on collision, then it would exist.

VIII. CONCLUSIONS AND DISCUSSIONS

We study here the nature of the toroidal single-particle states and their wave functions in the intermediate-mass region where negative shell corrections are expected. We find that toroidal shells occur with a regular structure in an extended region with many toroidal magic numbers at various toroidal deformations R/d. The enhanced stability associated with the nuclear shell effects suggests that there may be many exited toroidal states stable against expansion and contraction of the toroidal major radius.

Toroidal Routhian energies under the constraint of an angular momentum have been evaluated, and one finds regions of low Routhian energy density indicating that toroidal high-spin isomers may also have a common occurrence in the intermediate-mass region.

A new vorticity degree of freedom opens up for examination for toroidal nuclei in the intermediate-mass region. There can be vortex creating particle-hole excitations that will allow the nucleus to become a toroidal vortex nucleus with a net vorticity by promoting nucleons from states of vorticity of one sign to selectively populate unoccupied states with vorticities of the other sign.

To get more accurate locations of the toroidal shells, a more general potential such as those with a Wood–Saxon shape potential will be useful in determining the toroidal shell nucleon numbers and high-spin isomers. Future mean-field calculations in the intermediate-mass region will be of great interest to give reliable quantitative estimates of the energies of the toroidal isomers. From all indications and results from the present work, the intermediate-mass region hold the promise to be a rich region for the exploration of the toroidal degree of freedom.

There remain many interesting problems that will need to be considered in the future. The question of the decay of the toroidal nucleus, the stability against sausage distortions or the Plateau–Rayleigh instability [44–46], and the effects of the quantization of the spin on the sausage instability, will need to be addressed. There are also the questions of pairing interaction that may be weakened by the cranking of a pair having opposite tendencies in changing the energy, and the questions on the effects of self-consistent mean fields and the signatures for toroidal nuclei. These and many other unresolved questions make the study of toroidal nucleus a very interesting area for further investigation.

ACKNOWLEDGMENTS

The authors would like to thank Professor Yitzhak Sharon for helpful discussions. The research was supported in part by the Division of Nuclear Physics, US Department of Energy, under Contract DE-AC05-00OR22725.

APPENDIX: SOLUTION OF THE SINGLE-PARTICLE HAMILTONIAN

We would like to show how the eigenenergy of the single-particle state in Eq. (6) can be approximately solved. We split the spin-orbit interaction of Eq. (5) into two parts:

$$
\begin{aligned}
&-\frac{2\kappa\hbar}{m\mathring{\omega}_0}\boldsymbol{s}\cdot(\boldsymbol{\nabla}V_0\times\boldsymbol{p}) = V_{\rm so}^{\rm dia}+V_{\rm so}^{\rm off},\\
&V_{\rm so}^{\rm dia} = -\frac{\kappa\hbar}{m\mathring{\omega}_0}\begin{pmatrix}1 & 0\\ 0 & -1\end{pmatrix}\frac{\partial V_0}{\partial\rho}\frac{\hbar\partial}{i\rho\partial\phi},\\
&V_{\rm so}^{\rm off} = -\frac{\kappa\hbar}{m\mathring{\omega}_0}\left\{\begin{pmatrix}0 & e^{-i\phi}\\ e^{i\phi} & 0\end{pmatrix}\left(-\frac{\partial V_0}{\partial z}\frac{\hbar\partial}{i\rho\partial\phi}\right)\right.\\
&\qquad\left.+\begin{pmatrix}0 & -e^{-i\phi}\\ e^{i\phi} & 0\end{pmatrix}\left(-\frac{\partial V_0}{\partial\rho}\frac{\hbar\partial}{\partial z}+\frac{\partial V_0}{\partial z}\frac{\hbar\partial}{\partial\rho}\right)\right\}.
\end{aligned}
\tag{A1}
$$

For simplicity, we neglect the small contribution from the off-diagonal spin-orbit interaction because it gives higher-order transition matrix elements with a relatively large energy denominator. We consider therefore the approximate Hamiltonian

$$
H_0 = -\frac{\hbar^2}{2m}\nabla^2+V_0(\rho,z)+V_{\rm so}^{\rm dia},
\tag{A2}
$$

where

$$
V_{\rm so}^{\rm dia} = -\frac{2\kappa\hbar}{m\mathring{\omega}_0}\left(\frac{1}{\rho}\frac{\partial V_0}{\partial\rho}\right)s_zL_z = -\frac{2\kappa\hbar\omega_\perp^2}{\mathring{\omega}_0}\frac{\rho-R}{\rho}s_z\frac{\hbar\partial}{i\partial\phi}.
\tag{A3}
$$

We solve for eigenstates $|n_\rho n_z\Lambda_z\Omega_z\rangle$ of H_0,

$$
H_0|n_\rho n_z\Lambda_z\Omega_z\rangle = \epsilon(n_\rho n_z\Lambda_z\Omega_z)|n_\rho n_z\Lambda_z\Omega_z\rangle,
\tag{A4}
$$

normalized according to

$$
\int dz\,\rho d\rho\,d\phi\left|\hat{\mathcal{R}}_{n_\rho}(\rho)Z_{n_z}(z)\Phi_{\Lambda_z}(\phi)\right|^2\chi_{s_z}^\dagger\chi_{s_z} = 1.
\tag{A5}
$$

The two states with $\Omega_z=\Lambda_z+s_z=\pm|\Omega_z|$ have the same energy. They are degenerate. Writing out the operator explicitly, we get

$$
\begin{aligned}
&\left[-\frac{\hbar^2}{2m}\left(\frac{1}{\rho}\frac{\partial}{\partial\rho}\rho\frac{\partial}{\partial\rho}-\frac{\Lambda_z^2}{\rho^2}\right)+\frac{1}{2}m\omega_\perp^2(\rho-R)^2+V_{\rm so}^{\rm dia}\right]\\
&\quad\times\hat{\mathcal{R}}_{n_\rho}(\rho) = \epsilon^0_{n_\rho\Lambda_{n_z}\Omega_z}\hat{\mathcal{R}}_{n_\rho}(\rho),
\end{aligned}
\tag{A6}
$$

$$
\left[-\frac{\hbar^2}{2m}\frac{\partial^2}{\partial z^2}+\frac{1}{2}m\omega_\perp^2z^2-\epsilon^0_{n_z}\right]Z_{n_z}(z) = 0,
\tag{A7}
$$

$$
\left[i\frac{\partial}{\partial\phi}-\Lambda_z\right]\Phi_{\Lambda_z}(\phi) = 0.
\tag{A8}
$$

The single-particle eigenvalue is

$$\epsilon(n_\rho n_z \Lambda_z \Omega_z) = \epsilon^0_{n_\rho \Lambda_z \Omega_z} + \epsilon^0_{n_z}, \tag{A9}$$

so we can transform $\hat{\mathcal{R}}_{n_\rho}(\rho)$ in Eq. (A6) by

$$\mathcal{R}_{n_\rho}(\rho) = \sqrt{\rho}\hat{\mathcal{R}}_{n_\rho}(\rho). \tag{A10}$$

We normalize the single-particle wave function according to

$$\int dz \left|Z_{n_z}(z)\right|^2 = \int d\rho \left|\mathcal{R}_{n_\rho}(\rho)\right|^2 = \int d\phi \left|\Phi_{\Lambda_z}(\phi)\right|^2 = \chi^\dagger_{s_z}\chi_{s_z} = 1.$$

We obtain from Eq. (A6)

$$\left[-\frac{\hbar^2}{2m}\frac{\partial^2}{\partial\rho^2} + \frac{\hbar^2}{2m}\frac{\Lambda_z^2 - \frac{1}{4}}{\rho^2} + \frac{1}{2}m\omega^2(\rho - R)^2 + V^{\rm dia}_{\rm so}\right]\mathcal{R}(\rho) = \epsilon^0_{n_\rho\Lambda_z\Omega_z}\mathcal{R}(\rho). \tag{A11}$$

It is useful to make a change of coordinates:

$$q = \rho - R. \tag{A12}$$

We expand ρ about R in powers of q and keep terms up to the second order in q/R. Equation (A11) becomes

$$\left\{-\frac{\hbar^2}{2m}\frac{\partial^2}{\partial q^2} + \frac{\hbar^2}{2m}\frac{\Lambda^2 - \frac{1}{4}}{R^2}\left[1 - \frac{2q}{R} + \frac{3q^2}{R^2}\right] + \frac{m\omega^2 q^2}{2} + V^{\rm dia}_{\rm so}\right\}\mathcal{R}(\rho) = \epsilon^0_{n_\rho\Lambda_z\Omega_z}\mathcal{R}(\rho). \tag{A13}$$

We can solve the approximate Hamiltonian in q. We have

$$s_z L_z = \frac{J_z^2 - \Lambda_z^2 - 1/4}{2} = \frac{\Omega_z^2 - \Lambda_z^2 - 1/4}{2}. \tag{A14}$$

We assume the large-radius R approximation with small d/R, and expand $(\frac{1}{\rho}\frac{\partial V_0}{\partial\rho})$ in powers of q up to q^2,

$$\left(\frac{1}{\rho}\frac{\partial V_0}{\partial\rho}\right) = m\omega_\perp^2\frac{(\rho - R)}{\rho} = m\omega_\perp^2\left(\frac{q}{R} - \frac{q^2}{R^2}\right). \tag{A15}$$

We also expand $(\Lambda^2 - 1/4)/\rho^2$ in power of q up to the second order of q,

$$\frac{\Lambda_z^2 - \frac{1}{4}}{\rho^2} = \frac{\Lambda_z^2 - \frac{1}{4}}{R^2}\left[1 - \frac{2q}{R} + \frac{3q^2}{R^2}\right]. \tag{A16}$$

The eigenvalue equation can be rewritten as

$$\left\{-\frac{\hbar^2}{2m}\frac{\partial^2}{\partial q^2} + \frac{\hbar^2}{2m}\frac{\Lambda_z^2 - \frac{1}{4}}{R^2} + \frac{1}{2}m\omega_\perp^2 q^2 + V^{(1)} - \epsilon^0_{n_\rho\Lambda_z\Omega_z}\right\} \times \mathcal{R}(\rho) = 0, \tag{A17}$$

where

$$V^{(1)}(q) = +\frac{\hbar^2}{2m}\frac{\Lambda_z^2 - \frac{1}{4}}{R^2}\left(-\frac{2q}{R} + \frac{3q^2}{R^2}\right) - \frac{2\kappa(\hbar\omega_\perp)^2}{\hbar\mathring{\omega}_0}s_z L_z\left(\frac{q}{R} - \frac{q^2}{R^2}\right).$$

We cast $\frac{1}{2}m\omega^2 q^2 + V^{(1)}(q)$ into a displaced quadratic form:

$$\tfrac{1}{2}m\omega^2 q^2 + V^{(1)}(q) = \tfrac{1}{2}m\omega_\perp'^2(q - q_0)^2 + a_0, \tag{A18}$$

where

$$\omega_\perp'^2 = \omega_\perp^2(1 + a_2), \tag{A19}$$

and a_0, a_2, and q_0 are given by

$$a_2 = \frac{\hbar^2}{2m}\frac{\Lambda_z^2 - \frac{1}{4}}{R^2}\frac{3}{\frac{1}{2}m\omega_\perp^2 R^2} + \frac{2\kappa(\hbar\omega_\perp)^2}{\hbar\mathring{\omega}_0}\frac{s_z\Lambda_z}{\frac{1}{2}m\omega_\perp^2 R^2}, \tag{A20}$$

$$a_0 = -\frac{1}{2}m\omega_\perp'^2 q_0^2, \tag{A21}$$

$$q_0 = -\frac{1}{2}a_1 R\left(\frac{\omega_\perp}{\omega_\perp'}\right)^2, \tag{A22}$$

$$a_1 = -\frac{\hbar^2}{2m}\frac{\Lambda_z^2 - \frac{1}{4}}{R^2}\frac{2}{\frac{1}{2}m\omega_\perp^2 R^2}\frac{s_z\Lambda_z}{\frac{1}{2}m\omega_\perp^2 R^2}. \tag{A23}$$

Equation (A17) becomes

$$\left\{-\frac{\hbar^2}{2m}\frac{\partial^2}{\partial q^2} + \frac{\hbar^2}{2m}\frac{\Lambda_z^2 - \frac{1}{4}}{R^2} + \frac{1}{2}m\omega_\perp'^2(q - q_0)^2 + a_0 - \epsilon^0_{n_\rho\Lambda_z\Omega_z}\right\}\mathcal{R}(\rho) = 0. \tag{A24}$$

The above eigenenergy solution for the ρ degree of freedom is

$$\epsilon^0_{n_\rho\Lambda_z\Omega_z} = \frac{\hbar^2}{2m}\frac{\Lambda_z^2 - \frac{1}{4}}{R^2} + \left(n_\rho + \frac{1}{2}\right)\hbar\omega_\perp' + a_0. \tag{A25}$$

After substituting the above eigenvalue into Eq. (A9), we get the single-particle energy given by Eq. (6),

$$\epsilon(n_\rho n_z \Lambda_z \Omega_z) = \left(n_\rho + \frac{1}{2}\right)\hbar\omega_\perp' + \left(n_z + \frac{1}{2}\right)\hbar\omega_\perp + \frac{\hbar^2}{2m}\frac{\Lambda_z^2 - \frac{1}{4}}{R^2} + a_0. \tag{A26}$$

[1] J. A. Wheeler, *Nucleonics Notebook* (unpublished, 1950); see also p. 297 in G. Gamow, *Biography of Physics* (Harper & Brothers Publishers, New York, 1961); R. Uwenma and J. A. Wheeler (unpublished); Princeton University Graduate Course Physics 576 Take-Home Examination Problem 2, May 22, 1963 (unpublished).

[2] C. Y. Wong, Toroidal nuclei, Phys. Lett. B **41**, 446 (1972).

[3] C. Y. Wong. Toroidal and spherical bubble nuclei, Ann. Phys. (NY) **77**, 279 (1973).

[4] C. Y. Wong, Superheavy toroidal nuclei, in *Superheavy Elements*, edited by M. A. K. Lodhi (Pergamon Press, New York, 1978), p. 524.

[5] C. Y. Wong, Rotating toroidal nuclei, Phys. Rev. C **17**, 331 (1978).

[6] C. Y. Wong, Hot Toroidal and Bubble Nuclei, Phys. Rev. Lett. **55**, 1973 (1985).

[7] Z. Y. Zhang and C. Y. Wong, Hot rotating toroidal nuclei, Phys. Rev. C **34**, 1094 (1986).

[8] D. H. Wilkinson, Alpha-neutron rings and chains, Nucl. Phys. A **452**, 296 (1986).

[9] H. M. Xu, J. B. Natowitz, C. A. Gagliardi, R. E. Tribble, C. Y. Wong, and W. G. Lynch, Formation and decay of toroidal and bubble nuclei and the nuclear equation of state, Phys. Rev. C **48**, 933 (1993).

[10] H. M. Xu, C. A. Gagliardi, R. E. Tribble, and C. Y. Wong, Fragmentation barriers of toroidal and bubble nuclei, Phys. Rev. C **49**, R1778 (1994).

[11] M. Warda, Toriodal structure of super-heavy nuclei in the HFB theory, Int. J. Mod. Phys. E **16**, 452 (2007).

[12] X. Viñas, M. Centelles, and M. Warda, Semiclassical description of exotic nuclear shapes, Int. J. Mod. Phys. E **17**, 177 (2008).

[13] A. Staszczak and C.-Y. Wong, Toroidal super-heavy nuclei in Skyrme–Hartree–Fock approach, Acta Phys. Pol. B **40**, 753 (2009).

[14] W. Zhang, H.-Z. Liang, S.-Q. Zhang, and J. Meng, Search for ring-like nuclei under extreme conditions, Chin. Phys. Lett. **27**, 102103 (2010).

[15] T. Ichikawa, J. A. Maruhn, N. Itagaki, K. Matsuyanagi, P. G. Reinhard, and S. Ohkubo, Existence of an Exotic Torus Configuration in High-Spin Excited States of ^{40}Ca, Phys. Rev. Lett. **109**, 232503 (2012).

[16] T. Ichikawa, K. Matsuyanagi, J. A. Maruhn, and N. Itagaki, High-spin torus isomers and their precession motions, Phys. Rev. C **90**, 034314 (2014).

[17] A. Staszczak and C. Y. Wong, A region of high-spin toroidal isomers, Phys. Lett. B **738**, 401 (2014).

[18] A. Staszczak and C. Y. Wong, Particle-hole nature of the light high-spin toroidal isomers, Acta Phys. Pol. B **46**, 675 (2015).

[19] A. Staszczak and C. Y. Wong, Toroidal high-spin isomers in light nuclei with N not equal to Z, Phys. Scr. **90**, 114006 (2015).

[20] A. Staszczak and C. Y. Wong, Theoretical studies of possible toroidal high-spin isomers in the light-mass region, EPJ Web Conf. **117**, 04008 (2016).

[21] J. Meng, J. Peng, S. Q. Zhang, and P. W. Zhao, Solving Dirac equations on a 3D lattice with inverse Hamiltonian and spectral methods, Front. Phys. **8**, 55 (2013).

[22] Z. X. Ren, S. Q. Zhang, and J. Meng, Solving Dirac equations on a 3D lattice with inverse Hamiltonian and spectral methods, Phys. Rev. C **95**, 024313 (2017).

[23] P. W. Zhao, Z. P. Li, J. M. Yao, and J. Meng, New parametrization for the nuclear covariant energy density functional with a point-coupling interaction, Phys. Rev. C **82**, 054319 (2010).

[24] G. A. Lalazissis, T. Niksic, D. Vretenar, and P. Ring, New relativistic mean-field interaction with density-dependent meson-nucleon couplings, Phys. Rev. C **71**, 024312 (2005).

[25] A. Kosior, A. Staszczak, and C. Y. Wong, Superheavy toroidal nuclei in the Skyrme energy functional framework, Acta Phys. Pol. B Proc. Suppl. **10**, 249 (2017).

[26] A. Staszczak, C. Y. Wong, and A. Kosior, Toroidal high-spin isomers in the nucleus ^{304}120, Phys. Rev. C **95**, 054315 (2017).

[27] A. Kosior, A. Staszczak, and C. Y. Wong, Properties of superheavy isotopes $Z = 120$ and isotones $N = 184$ within the Skyrme-HFB model, Acta Phys. Pol. B Proc. Suppl. **11**, 167 (2018).

[28] X. G. Cao, E. J. Kim, K. Schmidt, K. Hagel, M. Barbui, J. Gauthier, S. Wuenschel, G. Giuliani, M. R. D. Rodriguez, S. Kowalski, H. Zheng, M. Huang, A. Bonasera, R. Wada, G. Q. Zhang, C. Y. Wong, A. Staszczak, Z. X. Ren, Y. K. Wang, S. Q. Zhang, J. Meng, and J. B. Natowitz, Evidence for high excitation energy resonances in the 7 alpha disassembly of ^{28}Si, arXiv:1801.07366.

[29] A. V. Afanasjev, S. E. Agbemava, and A. Gyawali, Hyperheavy nuclei: Existence and stability, Phys. Lett. B **782**, 533 (2018).

[30] K. Hagel *et al.*, Violent collisions and multifragment final states in the ^{40}Ca + ^{40}Ca reaction at 35 MeV/nucleon, Phys. Rev. C **50**, 2017 (1994).

[31] Y. Larochelle, L. Beaulieu, G. Anctil, B. Djerroud, D. Dore, R. Laforest, J. Pouliot, R. Roy, M. Samri, C. St-Pierre, G. C. Ball, D. R. Bowman, A. Galindo-Uribarri, E. Hagberg, D. Horn, D. Guinet, and P. Lautesse, Dependence of intermediate mass fragment production on the reaction mechanism in light heavy-ion collisions at intermediate energy, Phys. Rev. C **53**, 823 (1996).

[32] S. Wuenschel, K. Hagel, R. Wada, J. B. Natowitz, S. J. Yennello, Z. Kohley, C. Bottosso, L. W. May, W. B. Smith, D. V. Shetty, B. C. Stein, S. N. Soisson, and G. Prete, NIMROD-ISiS, a versatile tool for studying the isotopic degree of freedom in heavy ion collisions, Nucl. Instrum. Methods Phys. Res., Sect. A **604**, 578 (2009).

[33] R. Wada, T. Keutgen, K. Hagel, Y. G. Ma, J. Wang, M. Murray, L. Qin, P. Smith, J. B. Natowitz, R. Alfarro, J. Cibor, M. Cinausero, Y. ElMasri, D. Fabris, E. Fioretto, A. Keksis, S. Kowalski, M. Lunardon, A. Makeev, N. Marie, E. Martin, Z. Majka, A. Martinez-Davalos, A. Menchaca-Rocha, G. Nebbia, G. Prete, V. Rizzi, A. Ruangma, D. V. Shetty, G. Souliotis, P. Staszel, M. Veselsky, G. Viesti, E. M. Winchester, S. J. Yennello, W. Zipper, and A. Ono, Reaction dynamics and multifragmentation in Fermi energy heavy ion reactions, Phys. Rev. C **69**, 044610 (2004).

[34] W. Lin, X. Liu, M. R. D. Rodrigues, S. Kowalski, R. Wada, M. Huang, S. Zhang, Z. Chen, J. Wang, G. Q. Xiao, R. Han, Z. Jin, J. Liu, P. Ren, F. Shi, T. Keutgen, K. Hagel, M. Barbui, C. Bottosso, A. Bonasera, J. B. Natowitz, T. Materna, L. Qin, P. K. Sahu, and H. Zheng, Experimental reconstruction of primary hot isotopes and characteristic properties of the fragmenting source in heavy-ion reactions near the Fermi energy, Phys. Rev. C **90**, 044603 (2014).

[35] W. Cassing, Dynamical aspects of intermediate-energy nucleus-nucleus collisions, Z. Phys. A **327**, 87 (1987).

[36] A. Ono, Antisymmetrized molecular dynamics with quantum branching processes for collisions of heavy nuclei, Phys. Rev. C **59**, 853 (1999).

[37] R. J. Charity, A systematic description of evaporation spectra for light and heavy compound nuclei, Phys. Rev. C **82**, 014610 (2010).

[38] D. Mancusi, R. J. Charity, and J. Cugnon, Unified description of fission in fusion and spallation reactions, Phys. Rev. C **82**, 044610 (2010).

[39] D. Lacroix, A. Van Lauwe, and D. Durand, Event generator for nuclear collisions at intermediate energies, Phys. Rev. C **69**, 054604 (2004).

[40] M. Brack, J. Damgaard, A. S. Jensen, H. C. Pauli, V. Strutinsky, and C. Y. Wong, Funny hills: The shell-correction approach to

nuclear shell effects and its applications to the fission process, Rev. Mod. Phys. **44**, 320 (1973).

[41] A. Bohr and B. R. Mottelson, The structure of angular momentum in rapidly rotating nuclei, Nucl. Phys. A **354**, 303c (1981).

[42] S. G. Nilsson, C. F. Tsang, A. Sobiczewski, Z. Szymański, S. Wycech, C. Gustafson, I.-L. Lamm, P. Möller, and B. Nilsson, On the nuclear structure and stability of heavy and superheavy elements, Nucl. Phys. A **131**, 1 (1969).

[43] P. Ring and P. Schuck, *The Nuclear Many-Body Problem* (Springer-Verlag, Berlin, Heidelberg, New York, 1980), p. 142.

[44] J. Plateau, *Experimental and Theoretical Researches on the Figures of Equilibrium of a Liquid Mass withdrawn from the Action of Gravity*, Annual Report of the Board of Regents of the Smithsonian Institution, 207 (1863); *ibid.* 285 (1864); *ibid.* 411 (1865); *ibid.* 255 (1866).

[45] Lord Rayleigh, The equilibrium of revolving liquid under capillary force, Philos. Mag. **28**, 161 (1914).

[46] J. Eggers, Nonlinear dynamics and breakup of free-surface flows, Rev. Mod. Phys. **69**, 865 (1997).

[47] D. Suzuki, M. Ford, D. Bazin, W. Mittig, W. G. Lynch, T. Ahn, S. Aune, E. Galyaev, A. Fritsch, J. Gilbert, F. Montes, A. Shore, J. Yurkon, J. J. Kolata, J. Browne, A. Howard, A. L. Roberts, and X. D. Tang, Prototype AT-TPC: Toward a new generation active target time projection chamber for radioactive beam experiments, Nucl. Instrum. Methods Phys. Res., Sect. A **691**, 39 (2012); D. Suzuki, A. Shore, W. Mittig, J. J. Kolata, D. Bazin, M. Ford, T. Ahn, F. D. Becchetti, S. Beceiro Novo, D. Ben Ali, B. Bucher, J. Browne, X. Fang, M. Febbraro, A. Fritsch, E. Galyaev, A. M. Howard, N. Keeley, W. G. Lynch, M. Ojaruega, A. L. Roberts, and X. D. Tang, Resonant α scattering of ^{6}He: Limits of clustering in ^{10}Be, Phys. Rev. C **87**, 054301 (2013).

[48] T. Roger, M. Caamano, C. E. Demonchy, W. Mittig, H. Savajols, and I. Tanihata, Tracking algorithms for the active target MAYA, Nucl. Instrum. Methods Phys. Res., Sect. A **638**, 134 (2011).

[49] B. Ketzer (GEM-TPC and ALICE TPC Collaborations), A Time Projection Chamber for high-rate experiments: towards an upgrade of the ALICE TPC, Nucl. Instrum. Methods Phys. Res., Sect. A **732**, 237 (2013).

[50] Y. Ayyad *et al.*, Overview of the data analysis and new micropattern gas detector development for the Active Target Time Projection Chamber (AT-TPC) project, J. Phys.: Conf. Ser. **876**, 012003 (2017).

[51] D. Bazin, J. Bradt, Y. Ayyad, W. Mittig, T. Ahn, S. Beceiro-Novo, L. Carpenter, M. Cortesi, A. Fritsch, J. J. Kolata, W. Lynch, and N. Watwood, The Active Target Time Projection Chamber at NSCL, EPJ Web Conf. **163**, 00004 (2017).

[52] L.-G. Pang, H. Petersen, Qun Wang, and X.-N. Wang, Vortical Fluid and Λ Spin Correlations in High-Energy Heavy-Ion Collisions, Phys. Rev. Lett. **117**, 192301 (2016).

[53] W.-T. Deng and X.-G. Huang, Vorticity in heavy-ion collisions, Phys. Rev. C **93**, 064907 (2016).

[54] Yu. B. Ivanov and A. A. Soldatov, Vorticity in heavy-ion collisions at the JINR nuclotron-based ion collider facility, Phys. Rev. C **95**, 054915 (2017).

[55] Yu. B. Ivanov and A. A. Soldatov, Vortex rings in fragmentation regions in heavy-ion collisions at $\sqrt{s_{NN}} = 39$ GeV, Phys. Rev. C **97**, 044915 (2018).

[56] See, for example, https://apod.nasa.gov/apod/ap081104.html, *The Double Ring Galaxies of Arp 147 from Hubble*.

[57] Wikipedia, *List of Ring Galaxies*, https://en.wikipedia.org/wiki/List_of_ring_galaxies; see also http://chandra.harvard.edu/photo/2011/arp147/

[58] J. C. Theys and E. A. Spiegel, Ring galaxies, Astrophys. J. **208**, 650 (1976).

[59] B. F. Madore, E. Nelson, and K. Petrillo, Atlas and catalog of collisional ring galaxies, Astrophys. J., Suppl. Ser. **181**, 572 (2009).

[60] S. Rappaport, A. Levine, D. Pooley, and B. Steinhorn, Ultraluminous x-ray sources in Arp 147, Astrophys. J. **721**, 1348 (2010).